Corrosion behaviour of two Cu-based shape memory alloys in NaCl solution: an electrochemical study

Roberto Spotorno[a], Elisa Fracchia[b,c]*, Christian Krancher[d], Romina Krieg[d], Ralf Theiß[d], Peter Dültgen[d], Francesco Marco Pezzana[a], Federico Simone Gobber[c], Marco Actis Grande[c], Paolo Piccardo[a]

[a] Department of Chemistry and Industrial Chemistry, Università degli Studi di Genova, via Dodecaneso 31, 16146 Genoa, Italy (roberto.spotorno@unige.it, francescomarco.pezzana@gmail.com, paolo.piccardo@unige.it)

[b] Department of Management and Production Engineering (DIGEP), Politecnico di Torino, Viale Teresa Michel 5, Alessandria, Italy (elisa.fracchia@polito.it)

[c] Department of Applied Science and Technology (DISAT), Politecnico di Torino, Viale Teresa Michel 5, Alessandria, Italy (federico.gobber@polito.it, marco.actis@polito.it)

[d] Forschungsgemeinschaft Werkzeuge und Werkstoffe e.V., Papenberger Str. 49, 42859 Remscheid, Germany (krancher@fgw.de, krieg@fgw.de, Theiss@fgw.de, Dueltgen@fgw.de)

Correspondence: *elisa.fracchia@polito.it

Data Availability Statement

The raw/processed data required to reproduce these findings cannot be shared at this time as the data also forms part of an ongoing study.

Conflict of interest

The authors declare that they have no known competing financial interests or personal relationships that could have appeared to influence the work reported in this paper.

Abstract

The corrosion behaviour of two different Cu-Al-Mn-Ni alloys, pseudoelastic and pseudoplastic, was studied in a 0.6 M sodium chloride aqueous solution by monitoring the open-circuit potential for 100 hours and characterizing the resulting corrosion products. Electrochemical impedance spectroscopy analysis detected three processes related to the electrochemical double layer, a passive film, and a diffusive contribution associated with the dissolution/precipitation of corrosion products. Potentiodynamic scans revealed a cathodically controlled corrosion mechanism and the presence of active-passive behaviour at anodic potentials for both alloys studied. Polarisation of the samples at selected potentials in the anodic branch allowed the investigation of the reactions involved, highlighting an improved corrosion resistance of the pseudoelastic alloy. The corrosion rates of the pseudoelastic and pseudoplastic alloys, after 100 hours of immersion, were determined to be 0.007 mmpy and 0.011 mmpy, respectively. The post-experiment characterization was carried out by means of Scanning Electron Microscopy, micro-Raman spectroscopy and X-ray Diffraction, supporting the electrochemical results.

Keywords: Cu-based alloys, Martensite, Polarization, EIS, Micro-Raman spectroscopy, Anodic dissolution

1. Introduction

Shape memory alloys (SMAs) constitute a class of materials that can regain their original shape after deformation thanks to a lattice transformation process between two phases [1]. They undergo a reversible thermoelastic martensitic phase transformation in the solid state, which leads to a macroscopic shape change. The phase transformation is subject to a defined stress-temperature relationship between a high-temperature phase (austenite) and a low-temperature phase (martensite) [2,3].

The pseudoelastic behaviour describes the stress-induced martensitic phase transformation. In this case, the material is initially in the austenitic state. An externally applied mechanical load provides the driving force for the transformation to the martensitic material state. The transformation is reversed by relieving the load. In pseudoplastic behaviour, the material is present as twinned martensite. External stress causes the detwinning of martensite. When the load is removed, the deformation of the material is initially retained. Heating the material then leads to a complete deformation back to the original geometry because of the lattice transformation to the austenitic state and finally, cooling leads to a transformation back into twinned martensite [4,5].

The characteristic material behaviour is mainly used with binary Ni-Ti alloys in the field of medical engineering, but it is also utilized in automotive and aerospace applications [1,6]. These alloys have been investigated in detail in the past and are suitable for use at temperatures up to 100 °C due to their excellent shape memory properties, long lifetime and corrosion resistance [7,8]. Restrictions for the application of binary Ni-Ti alloys are due to limited transformation temperatures, high requirements on the melting technology, and high alloy costs [9,10].

Since shape memory behaviour also occurs in several other alloy systems, current developments are striving to develop alloys that bring both technological and economic advantages [11]. In recent years, researchers have been particularly interested in Cu-based SMAs. The reason for this is the wide achievable transformation temperature window, reduced alloying element costs, manageable

technical requirements for the melting technology, and increased formability and machinability. Possible fields of application are damping systems, medical and electrical devices with high thermal and electrical conductivity, microactuators, energy storage, and transition technologies. Considerable research attention has been directed toward Cu-Al-X SMAs [12,13]. The Cu-Al-Ni alloy system with high strengths and high transformation temperatures, depending on aluminium and nickel content, is investigated by several research groups. Depending on the amount of aluminium and nickel, different martensitic transformation sequences are observed [14,15]. A significant disadvantage of Cu-Al-Ni alloys is the large elastic anisotropy, which results in deficient thermo-mechanical behaviour due to local stress concentration at grain boundaries, leading to grain boundary cracking [16,17].

Several recent studies have reported that Cu-Al-Mn SMAs exhibit excellent ductility, high damping properties, and fatigue properties [18,19]. The work of Mallik and Sampath demonstrated the effect of aluminium and manganese concentration on transformation temperatures, strain recovery (shape memory effect), and pseudoelasticity [20]. Depending on the chemical composition of the alloy, two martensitic transformation sequences are observed in Cu-Al-Mn systems [21].

In a few studies, the effect of quaternary alloying elements on the microstructure and transformation temperature change was investigated as well as the advantageous combination of the characteristics of both alloy systems [22]. The addition of nickel to Cu-Al-Mn SMA and of Manganese to Cu-Al-Ni SMA, respectively, results in a change of transformation temperatures, phase transformation sequence, shape memory properties, microstructural characteristics, and mechanical material response, resulting in a wide transformation temperature window and a reasonable combination of mechanical characteristics [23–26].

An essential criterion for the use of SMAs is the material behaviour under the environmental conditions that occur in the specific field of application. The damage behaviour of the material is not only determined by the progressive functional and structural fatigue but is also influenced by the operating temperatures and ambient media. Thus, the effect of corrosive media must also be

considered for the utilization of SMAs. Substantial for the resulting material behaviour is the chemical composition and the microstructure. In particular, the differences in the microstructure of SMAs depending on the chemical composition must be considered.

Cu-based alloys are known to be subject to selective corrosion, which can lead to local changes in their chemical and mechanical properties [27]. When exposed to air, aluminium promotes the formation of an alumina barrier film, which is not effective in the presence of chloride ions being continuously dissolved to form aluminium chloride hydroxide [28]. Recent experimental studies have focused on the evaluation of the electrochemical properties of copper-based SMAs, with particular interest in the mechanisms of corrosion damage and stabilization of passivation layers [29,30].

Saud et al. reported that the addition of manganese in the range of 0.4 to 1.0 % resulted in higher corrosion resistance compared to ternary Cu-Al-Ni, due to a shift of the corrosion potential to the more noble direction, resulting in lower corrosion rates [31,32].

Other studies have shown that manganese promotes the formation of its oxides/hydroxides, which increase the passivity of the surface [31,33,34]. Nady et al. investigated that an increase in nickel content leads to an improvement in corrosion resistance because the nickel concentration on the surface increases and the vacancies in the copper (I) oxide layer decrease [35]. In contrast, Badawy et al. found that the presence of nickel in the alloy reduced the corrosion resistance, as the high nickel content on the surface of the alloy inhibits the formation of passivating compounds [36]. Vrsalovic et al. noted that a brief homogenization heat treatment improves the corrosion resistance of Cu-Al-Ni SMAs in NaCl solution and increases charge transfer resistance and surface layer resistance by EIS measurements [37,38].

In this work, the corrosion behaviour of two Cu-Al-Mn-Ni SMAs was studied by monitoring their open-circuit potential and electrochemical impedance spectroscopy evolution during a 100-hour immersion in a sodium chloride solution simulating the marine environment. In addition, detailed potentiodynamic polarisation combined with post-experiment using micro-Raman spectroscopy, X-

ray diffraction, and scanning electron microscopy was performed to discuss the electrochemical processes at the sample surface.

The current study aims to extend the knowledge of the corrosion behaviour of copper-based SMAs and to provide important insights into the factors affecting the durability of Cu-Al-Mn-Ni alloys. Such aspects should be considered for the development, fabrication, and utilization of reliable devices that can be used in practical SMA applications. Therefore, the study contributes to the identification of potential copper-based SMAs and their possible application in chloride-containing conditions, such as automotive applications under road salt conditions and marine applications.

2. Materials and Methods

2.1 Preparation of samples

Polycrystalline pseudoelastic and pseudoplastic Cu-Al-Mn-Ni SMA ingots with chemical compositions according to Table 1 were prepared by vacuum induction melting (VTC 200 V-Ti, Indutherm Erwärmungsanlagen GmbH, Germany) from the pure elements (purity ≥ 99.9 %). Melting was performed in a graphite crucible under vacuum conditions after purging twice with argon before heating, to minimize oxide formation. The molten alloys (1190 °C) were poured into a permanent steel mold preheated to 400 °C. Bars were cut from the casting, and a heat treatment (R50/500/12, Nabertherm GmbH, Germany) was conducted at 850 C for 30 min without a protective atmosphere. The Alloy#1 specimens were quenched with ice water, while the Alloy#2 samples were quenched with oil, to achieve the required shape memory properties and microstructure.

Table 1 reports the transformation temperatures of the heat-treated bars, namely martensite finish (M_f), martensite start (M_s), reverse transformation start (A_s) and reverse transformation finish (A_f). They were investigated by Differential Scanning Calorimetry (DSC 214 Polyma, NETZSCH-Gerätebau GmbH, Germany) with a heating and cooling rate of 10 $K \cdot min^{-1}$ within a temperature range

from -100 °C to 250 °C following ASTM F2004-17 (Standard Test Method for Transformation Temperature of Nickel-Titanium Alloys by Thermal Analysis).

Table 1. Chemical compositions and transformation temperatures of the Cu-Al-Mn-Ni SMAs

Sample	**Chemical composition (at. %)**				**Transformation temperatures (°C)**			
	Cu	Al	Mn	Ni	M_f	M_s	A_s	A_f
Alloy#1	Bal.	16.75	9.77	1.93	-32 ± 1	-28 ± 1	-18 ± 2	-9 ± 2
Alloy#2	Bal.	23.29	2.49	3.72	139 ± 2	167 ± 1	168 ± 1	186 ± 1

For this purpose, thin slices were cut from the bars with a diamond wire saw. Their weight was reduced by wet grinding to a range between 15 and 25 mg for the DSC specimens. The recorded DSC curves were evaluated according to the tangent method using the software "Protheus – Thermal Analysis" (NETZSCH-Gerätebau GmbH, Germany).

For the following characterization, the specimens of each alloy, namely Alloy#1 and Alloy#2, were cut into a cylindrical shape with a height of 1 cm and a base area of 1 cm^2. They were embedded in epoxy resin to allow automatic grinding and polishing of the base surface.

2.2 Electrochemical characterization

The samples for the electrochemical studies were ground with silicon carbide paper to a grit size of 1000 to remove corrosion products formed in air and to uniform the roughness of the surfaces exposed to the test solution.

Electrochemical characterization was performed in a naturally aerated aqueous 0.6 M sodium chloride solution (VWR, AnalaR NORMAPUR, purity > 99.5 %) at room temperature. Experiments were performed using a proprietary three-electrode cell suitable for exposing a fixed area of 1 cm^2 of

sample. The cell configuration consisted of a sample connected as a working electrode (WE), a reference electrode (RE) of Ag/ AgCl (KCl 3 M), and a platinum wire as a counter electrode (CE) in a volume of 0.250 L of test solution under static conditions.

Measurements were performed using a frequency response analyzer (SI 1260 Electrochemical Interface, Solartron Analytical, Farnborough, UK) coupled with a potentiostat/ galvanostat (SI 1287 Electrochemical Interface, Solartron Analytical, Farnborough, UK).

The Open Circuit Potential (OCP) of both alloys was recorded for 100 hours. In a separate experiment with the same duration, electrochemical impedance spectroscopy (EIS) was measured every 20 hours with an AC (alternate current) signal amplitude of ±10 mV in the frequency range from 200 kHz to 0.1 Hz at a frequency density of 10 points/decade.

The values of polarisation resistance (R_p) and corrosion current (I_{corr}) were estimated on additional samples for each alloy after 1 and 100 hours of immersion using the linear polarization resistance (LPR) technique, applying a sweep rate of 0.1 $mV \cdot s^{-1}$ in the potential range of ±40 mV versus OCP. Fitting was performed using CView® software (Scribner Associates Inc., Southern Pines, USA).

The average results obtained on two replicated samples for each measurement showed an experimental deviation of less than 5 % for both OCP and polarization analysis, which is not indicated in the plotted data, so the different trends depending on the system considered could be seen.

The EIS spectra were analyzed using the Differential Impedance Analysis (DIA) [39]. This method allows the identification of dispersed time constants by scanning the impedance data along the frequency coordinate (ω) using a local operating model (LOM). The LOM is conceptualized as a simple first-order inertial system, comprising a parallel arrangement of resistance (R) and capacitance (C). An additional term, representing the electrolyte resistance (R_s) in electrochemical systems, is incorporated in series. To enable a statistical approach in determining LOM parameters at every frequency, derivatives of the real and imaginary parts of impedance with respect to frequency are integrated into the initial 3D dataset (frequency, real part, and imaginary part). The parameters

resulting from the scanning procedure include the resistance, capacitance, and time constant, defined as $T_n = R_n \cdot C_n$, where R_n and C_n are the resistance and the capacitance of the n-th process, respectively. The distribution of such parameters can be represented versus the frequency coordinate in order to obtain information on the structure of the electrical equivalent circuit (EEC) of the system. The structural insights obtained through DIA were exploited to propose the EEC describing the corrosion systems and for quantitative parametric identification via Complex Non-linear Regression Least Squares (CNRLS).

The EIS spectra were fitted using the CNRLS method [40,41], with ZView® software (Scribner Associates Inc., Southern Pines, USA), accepting a fitting error of less than 1 % of the total spectrum and relative uncertainty of the individual elements of less than 30 %.

Polarisation curves were measured on additional samples after 1 hour of immersion in the test solution. These measurements consisted of potentiodynamic scans with a sweep rate of 0.5 $mV \cdot s^{-1}$ in the potential range of -1.2 to +0.8 V versus Ag/ AgCl. Based on the characteristics of the measured polarisation curves, additional samples were polarised at the same sweep rate with the scan stopped at fixed potentials (Table 2) to investigate the corrosion products formed at different points on the polarisation curves.

Table 2. Sample names and testing procedures.

Sample name	Procedure
Alloy#1-OCP, Alloy#2-OCP	Measurement of OCP for 100 hours and EIS each 20 hours
Alloy#1-A, Alloy#2-A	Measurement of OCP for 1 hour and polarization from OCP to -0.2V vs Ag/AgCl
Alloy#1-B, Alloy#2-B	Measurement of OCP for 1 hour and polarization from OCP to +0.2V vs Ag/AgCl
Alloy#1-C, Alloy#2-C	Measurement of OCP for 1 hour and polarization from OCP to +0.8V vs Ag/AgCl

2.3 Microstructural and post-experiment characterization

The specimens for microstructural characterization were ground and polished according to the metallographic standard procedure ASTM E 3-11 (Standard Guide for Preparation of Metallographic Specimens) to 1 μm diamond suspension and etched with a ferric chloride/hydrochloric acid/water solution (as indicated in E407 – 23 standard, Standard Practice for Microetching Metals and Alloys) to observe their microstructure and to compare it with the post-corrosion aspects.

The microstructure of the samples was studied using an inverted metallographic light microscope (OM, Leica MEF 4M, Leica Microsystems GmbH, Wetzlar, Germany) equipped with a digital camera for image acquisition (Zeiss AxioCam MRc 5, Carl Zeiss, Oberkochen, Germany) and through a stereomicroscope (Leica Microsystems MS5, Leica Microsystems GmbH, Wetzlar, Germany).

Chemical analyses of the studied samples were performed by a micro-Raman spectroscope (InVia Raman Microscope, Renishaw, Wotton-under-Edge, United Kingdom) equipped with a solid-state laser of 532 nm and by the X-ray diffractometer (Empyrean, Malvern Panalytical, Malvern, United Kingdom), using 2θ of 10° to 80°, step size 0.013° and a Cu anode and finally through and energy dispersion X-ray spectroscope (EDXS; Cambridge INCA 300 with PentaFET EDXS detector; Oxford Instruments Oxfordshire, U.K. sensitive to light elements, $Z > 5$) in conjunction with a scanning electron microscope (SEM; Zeiss Evo40; Carl Zeiss, Oberkochen, Germany).

3. Results

3.1 Microstructural characterization of the alloy

Table 1 reports the average chemical composition of the tested alloys. Alloy#1 is characterized by a lower percentage of aluminium and nickel, but a higher percentage of manganese compared to Alloy#2. The typical pseudoelastic microstructure of Alloy#1 shown in Figure 1a consists of coarse polygonal grains with a secondary needle-like phase visible at their boundaries. XRD analysis on polished surface indicated the presence of three aluminium-manganese phases, aluminium copper

and copper-nickel phases; Alloy#2 (Figure 1b) is characterized by coarse primary grains with a complete martensitic structure inside. This microstructure is representative of a pseudoplastic material state and is characterized by the orthorhombic aluminium-copper and the monoclinic aluminium-copper-nickel phases.

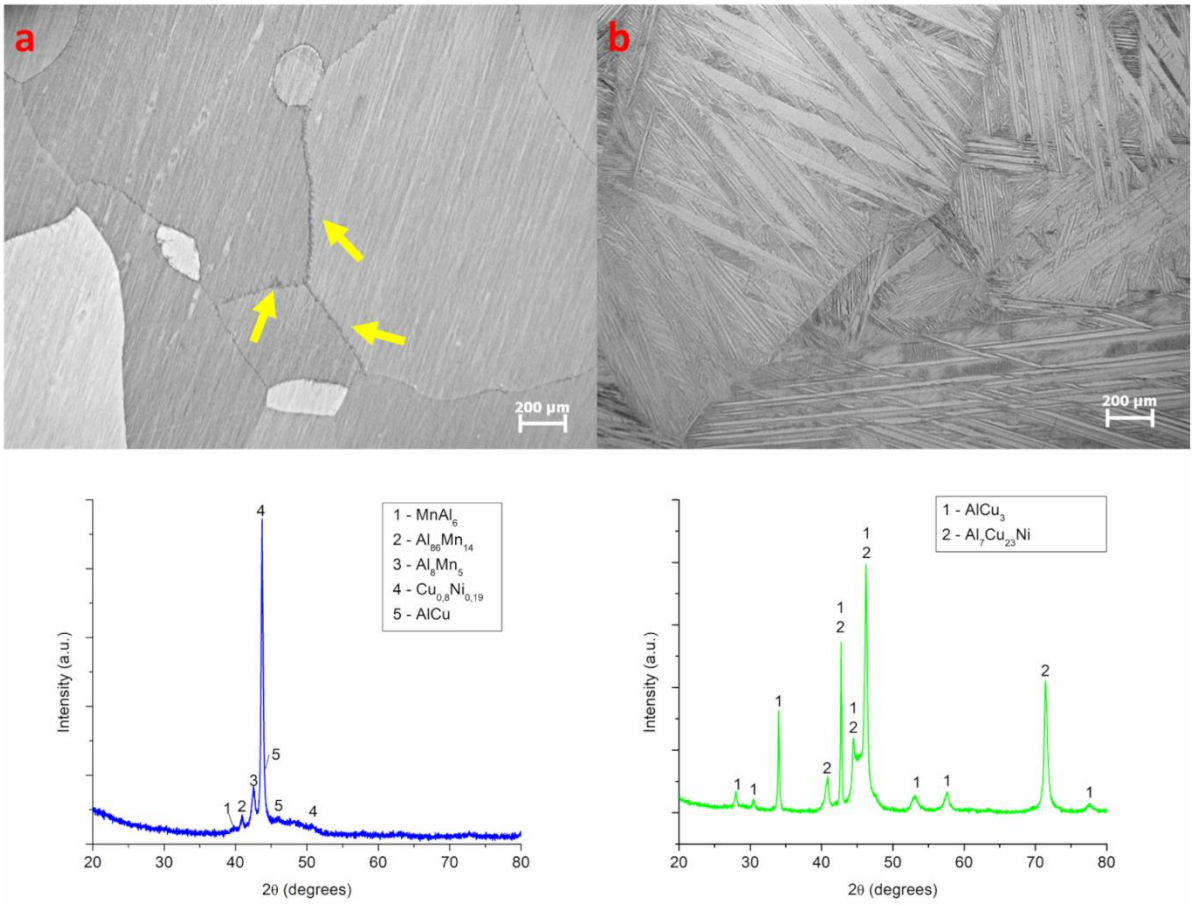

Figure 1. Optical micrographs and XRD spectra of (a) Alloy#1 and (b) Alloy#2, both polished and etched. Arrows in (a) indicate the secondary phase visible at the grain boundaries.

3.2 Electrochemical characterization

Open circuit potential

When the samples of the two alloys were immersed in the test solution, the initial OCP values decreased by about 25 mV in the first 5 hours, then their trends developed in opposite directions (Figure 2). Alloy#1 exhibited lower initial values, which then increased, exceeding those of Alloy#2

after 15 hours of immersion. During the first 40 hours of the experiment, the OCP of Alloy#1 increased, reaching stable values between 40 and 80 hours, despite some potential fluctuations. The last 20 hours of immersion were characterized by a slight potential decrease. The potential of Alloy#2 steadily decreased for the whole test duration. A comparison of the two OCP profiles highlights higher potential fluctuation for the Alloy#1, especially during the first 40 hours, suggesting a connection to the evolution of the corrosion products on the surface and the completion of its coverage.

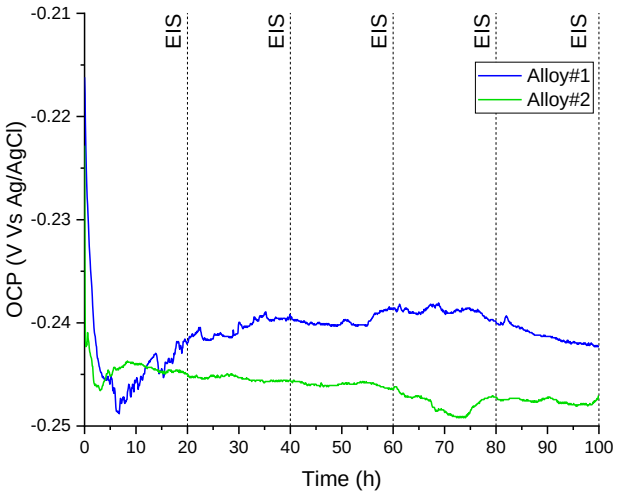

Figure 2. Open Circuit Potential of Cu-Al-Mn-Ni SMA samples depending on time.

Electrochemical Impedance Spectroscopy (EIS)

Impedance measurements were performed to investigate the electrochemical properties of the alloy/solution interface and to evaluate the effects of the presence of any corrosion products. The method involves the use of alternating currents of varying frequencies to distinguish the time constants of the individual processes in the system under investigation.

The resistive and capacitive contributions can be derived from the EIS spectra, presented in Nyquist plots (Figure 3a and Figure 3c), that show the real and imaginary parts of the electrical response of the samples. The real part is associated with resistive contributions, while the imaginary part is

associated with capacitive or inductive contributions. The combination of both contributions allows the interpretation of the measurement by fitting an electrical equivalent circuit (EEC), describing the processes at the alloy/solution interface.

The data representation in Bode plots (Figure 3b and Figure 3d) is used to observe the distribution of impedance phase over the measured frequency range. This information complements the Nyquist plot and is typically used to support the EIS interpretation by identifying the number of processes in the measured spectrum, distinguishable as peaks in the Bode plots, and their frequency ranges.

The phase of all measured spectra tends to 0 at the high-frequency end, indicating the presence of a pure resistive contribution that, in liquid media, is attributable to the solution resistance. The value of such contribution is commonly measured as the first intercept of the spectra, represented in Nyquist plots, with the real part axis. Decreasing the frequency, the phase tends to have more negative values indicating the presence of capacitive contributions, considering that for pure capacitance the phase angle equals -90°. This behaviour is observable for all measurements but with differences in the frequency dependency of the phase angle for each spectrum. In particular, the first measurements, performed after 1 hour of immersion, exhibited for both alloys two overlapped peaks, thus indicating two distinct time constants that in the Nyquist plots correspond to the first semicircular shape, measured for both samples after 1 hour of immersion.

The size of the diameter of the semicircles in the Nyquist plots reflects on the corrosion reactions and the passivation capacity of films formed on the surface of the samples, that is, the larger the diameter, the greater the corrosion resistance [42].

For frequencies below 0.1 Hz, the phase is stabilizing at values of -35° for Alloy#1 and -30° for Alloy#2, indicating a third process that in the Nyquist plot is represented as a tail with a slope of about 45°. In the following measurements, the size of the high-frequency semicircle visible in the Nyquist plot increased until it completely included the low-frequency tail, thus indicating a change in the EEC consisting of the elimination of the time constant related to the third process.

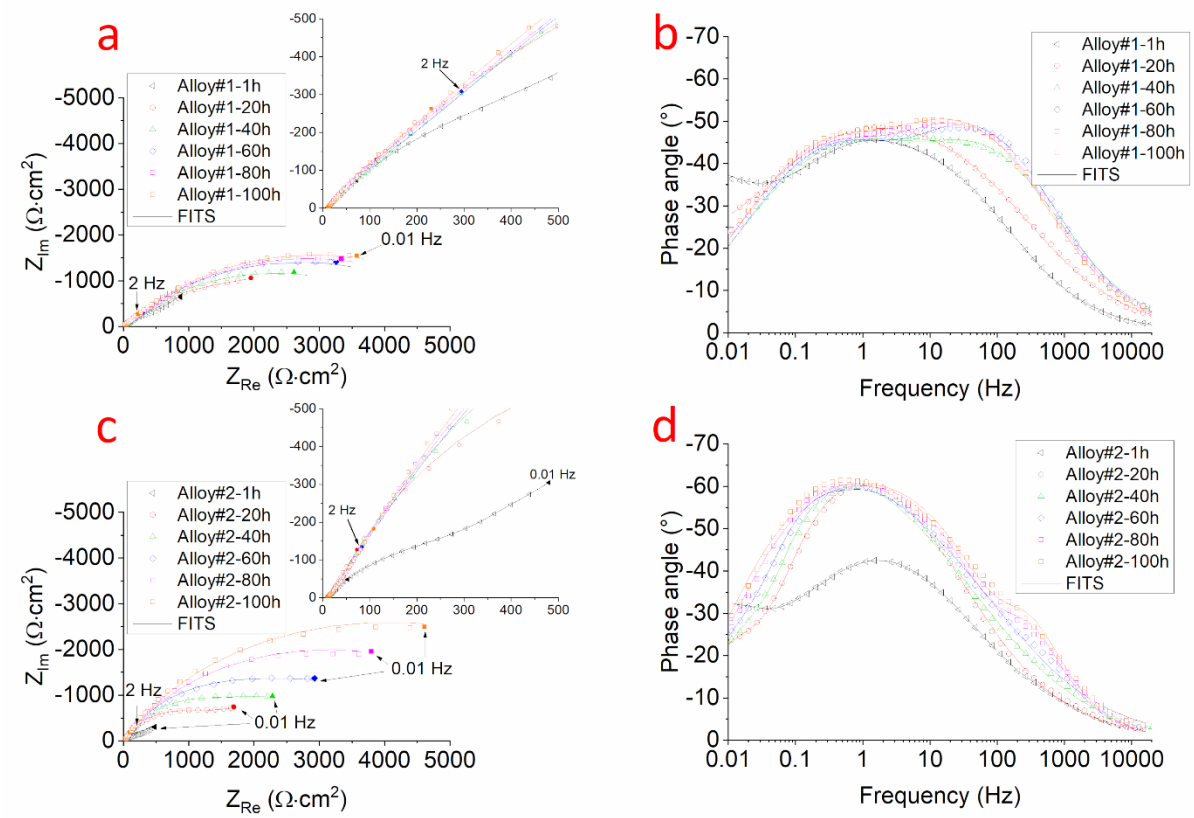

Figure 3. Nyquist plot of the electrochemical impedance spectroscopy (a, c) and the Bode representations (b, d).

To confirm the observations on the phase angle profiles and to obtain detailed information on the distribution of the impedance parameters, EIS spectra were analyzed using the DIA. Figure 4 (a and b) reports the LOM parameters (T, R, C) distribution in the whole frequency range for representative measurements highlighting the changes of the EEC describing the system. Both alloys showed a similar distribution of the LOM parameters at the beginning of the experiment. The absence of plateaus indicates that frequency-invariant processes, described by R//C meshes, are not present in the system [43]. The time constant profile allows a clear distinction between three segments (separated by local minima, marked with vertical dashed lines). Each segment can be associated to a

process for the construction of the EEC. After 60 hours of experiment, the last two segments were not anymore distinguishable, indicating the presence of only two time constants characterizing the EEC.

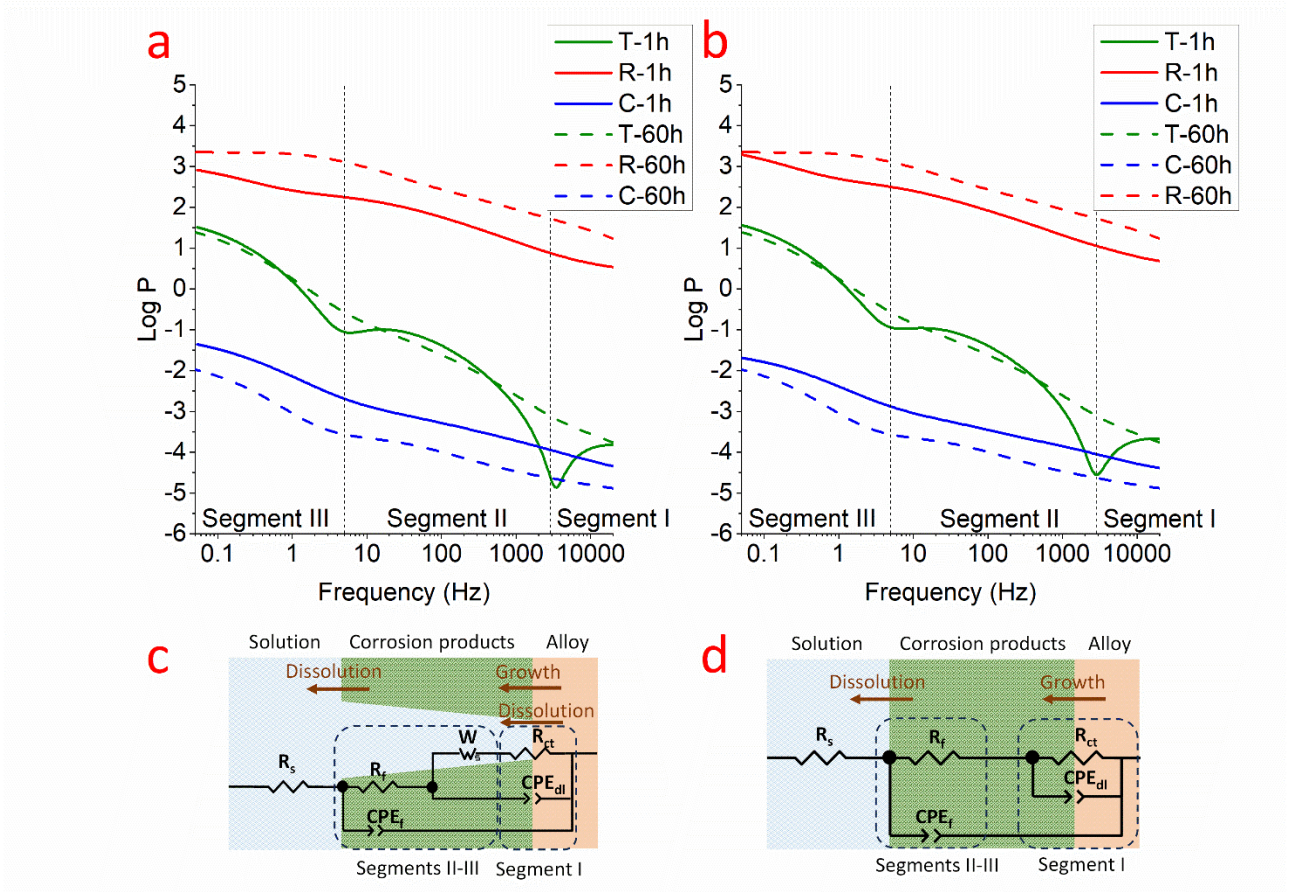

Figure 4. DIA temporal plots of EIS measured at 1 h and 60 h of Alloy#1 (a) and Alloy#2 (b), and the proposed EECs (c, d).

The EEC describing the first 40 hours of immersion is represented in Figure 4c, where the first resistance, R_s, describes the solution resistance while the two meshes in a ladder-type circuit describe the sequential processes occurring at the interface [44]. It is worth noting that constant-phase elements (CPE) are used in the circuit instead of capacitors. Such elements are commonly introduced in EECs to describe processes where the capacitance contribution is not ideal but dependent on frequency, as suggested by DIA profiles. The impedance of a CPE follows the equation below:

$$Z_{CPE} = \frac{1}{Q(j \cdot \omega)^n} \quad (1)$$

Where Q and n are coefficients, the first one is proportional to the capacitance of the process, while the second describes the divergency of the CPE from the ideal capacitor behaviour. When n < 1, the CPE time constant is frequency-dependent; when n = 1, the time constant becomes frequency-independent, and the CPE can be considered as a capacitor. The electrochemical systems commonly exhibit non-ideal capacitive behaviour and require the use of CPE to fit their EIS measurements due to inhomogeneities of their interfaces in terms of roughness, porosity, and composition [45].

The internal circuital mesh, R_{ct}/CPE_{dl} is used to model the charge transfer resistance and the double-layer capacitance, typically measured in the high-frequency range. To confirm this attribution, the effective capacitance of each CPE in the system was calculated using the Brug equation [46]:

$$C_{eff} = Q^{\frac{1}{n}} \cdot \left(\frac{1}{R_s} + \frac{1}{R_{ct}}\right)^{\left(\frac{n-1}{n}\right)} \quad (2)$$

Where Q and n are the CPE parameters. Based on the results shown in Table 3 and Table 4, the CPE with lower C_{eff} resulted attributable to the double layer capacitance being closer to the values experimentally measured by Khademi et al. at the same NaCl concentration of this work [47].

The R_f/CPE_f in the external mesh of the EEC is used to model the electrical properties of the film formed on the surface of the sample, constituted by corrosion products. The low-frequency tail measured in the first hours of the experiment indicates the presence of a diffusion-controlled phenomenon that can be fitted using a Warburg impedance element. As the CPE, this element is characterized by a frequency-dependent time constant whose impedance is defined by the following equation:

$$Z_W = R \cdot \frac{\tanh\left[(j \cdot T \cdot \omega)^P\right]}{(j \cdot T \cdot \omega)^P} \quad (3)$$

The variable T is equal to L^2 / D. The parameters L and D are the effective diffusion thickness and the effective diffusion coefficient of the ions, respectively. P is a coefficient depending on the time constant distribution [44]. Such an element describes diffusive phenomena occurring at the alloy/solution interface [48,49].

During the first 40 hours of the experiment, the diffusive resistance decreased for both alloys in favour of the charge transfer resistance, which increased to the extent that it overlapped the Warburg contribution after 60 hours. This is visible by the changes in the time constant profiles of figures 4a and 4b, but also by observing the Nyquist plots (Figures 3a and 3c), where the low-frequency tail gradually disappeared in the first three spectra for both alloys. Therefore, the EEC used to fit the spectra from 60 to 100 hours excludes the diffusive contribution, and it is constituted by only two time constants, related to the corrosion products film and the double layer (Figure 4d). For Alloy#1, the resistance of the film quickly increased from 8 to 48.5 Ω·cm^2 in the first 20 hours, it stabilized at values around 63 Ω·cm^2 and increased again with a linear trend reaching 94 Ω·cm^2. On the other hand, the film resistance of Alloy#2 kept stable values of about 10 Ω·cm^2 for the whole test duration. The charge transfer resistance started with values of 398 Ω·cm^2 for Alloy#1 and 167 Ω·cm^2 in Alloy#2 after 1 hour of immersion and increased by one order of magnitude in the following 40 hours, becoming the predominant process of the polarization resistance of both samples. For Alloy#1, R_{ct} stabilized after 60 hours at values higher than 5 kΩ·cm^2 while a linear increase was measured for Alloy#2, which reached 7.9 kΩ·cm^2 in 100 hours.

Table 3. EIS parameters obtained by fitting the spectra measured for Alloy#1 (C_{eff} columns have been calculated using the equation 2).

Alloy #1 Time (h)	R_s ($\Omega \cdot cm^2$)	R_f ($\Omega \cdot cm^2$)	CPE_f-T ($\Omega^{-1} \cdot cm^{-2} \cdot s^{n-1}$)	C_{eff} ($F \cdot cm^{-2}$)	CPE_f-P	R_{ct} ($\Omega \cdot cm^2$)	CPE_{dl}-T ($\Omega^{-1} \cdot cm^{-2} \cdot s^{n-1}$)	C_{eff} ($F \cdot cm^{-2}$)	CPE_{dl}-n	Ws-R ($\Omega \cdot cm^2$)	Ws-P
1	9.65	8.0	$7.695 \cdot 10^{-3}$	$1.343 \cdot 10^{-3}$	0.66	398.1	$3.311 \cdot 10^{-3}$	$7.998 \cdot 10^{-4}$	0.67	3900	0.51
20	9.81	48.5	$1.629 \cdot 10^{-3}$	$7.482 \cdot 10^{-4}$	0.85	1509	$1.804 \cdot 10^{-3}$	$6.548 \cdot 10^{-4}$	0.69	2361	0.46
40	10.34	62.1	$1.079 \cdot 10^{-3}$	$1.154 \cdot 10^{-4}$	0.68	4339	$7.723 \cdot 10^{-4}$	$1.163 \cdot 10^{-4}$	0.61	73.80	0.55
60	10.39	63.9	$5.276 \cdot 10^{-4}$	$1.310 \cdot 10^{-4}$	0.79	5132	$6.494 \cdot 10^{-4}$	$1.060 \cdot 10^{-4}$	0.63	-	-
80	10.36	80.7	$8.670 \cdot 10^{-4}$	$1.440 \cdot 10^{-4}$	0.73	5303	$6.883 \cdot 10^{-4}$	$1.337 \cdot 10^{-4}$	0.63	-	-
100	10.36	94.0	$1.063 \cdot 10^{-4}$	$1.538 \cdot 10^{-4}$	0.70	5480	$6.789 \cdot 10^{-4}$	$1.485 \cdot 10^{-4}$	0.64	-	-

Table 4. EIS parameters obtained by fitting the spectra measured for sample Alloy#2 (C_{eff} columns have been calculated using the equation 2).

Alloy#2 Time (h)	R_s ($\Omega \cdot cm^2$)	R_f ($\Omega \cdot cm^2$)	CPE_f-T ($\Omega^{-1} \cdot cm^{-2} \cdot s^{n-1}$)	C_{eff} ($F \cdot cm^{-2}$)	CPE_f-P	R_{ct} ($\Omega \cdot cm^2$)	CPE_{dl}-T ($\Omega^{-1} \cdot cm^{-2} \cdot s^{n-1}$)	C_{eff} ($F \cdot cm^{-2}$)	CPE_{dl}-n	Ws-R ($\Omega \cdot cm^2$)	Ws-P
1	9.52	9.9	$3.847 \cdot 10^{-2}$	$3.308 \cdot 10^{-2}$	0.92	167.0	$5.926 \cdot 10^{-3}$	$1.632 \cdot 10^{-3}$	0.64	2021	0.49
20	9.99	12.8	$2.519 \cdot 10^{-2}$	$2.371 \cdot 10^{-2}$	0.97	1105	$1.617 \cdot 10^{-3}$	$1.031 \cdot 10^{-3}$	0.88	1307	0.51
40	9.74	9.9	$1.830 \cdot 10^{-3}$	$1.069 \cdot 10^{-4}$	0.62	2952	$1.142 \cdot 10^{-3}$	$2.968 \cdot 10^{-4}$	0.74	718.0	0.50
60	9.34	9.6	$1.090 \cdot 10^{-3}$	$9.803 \cdot 10^{-5}$	0.69	4332	$1.011 \cdot 10^{-3}$	$2.447 \cdot 10^{-4}$	0.74	-	-
80	9.31	10.1	$8.282 \cdot 10^{-4}$	$1.038 \cdot 10^{-4}$	0.73	6077	$8.728 \cdot 10^{-4}$	$2.087 \cdot 10^{-4}$	0.74	-	-
100	9.37	11.1	$8.176 \cdot 10^{-4}$	$1.000 \cdot 10^{-4}$	0.72	7900	$7.608 \cdot 10^{-4}$	$1.700 \cdot 10^{-4}$	0.74	-	-

Potentiodynamic measurements

The LPR measurements were carried out to calculate the electrochemical parameters and compare the corrosion resistance of both samples. The I_{corr} values were obtained by fitting the data measured in the range ±40 mV vs OCP and are reported in Table 5. Using such parameters, the polarization resistance, R_p, was calculated for both samples according to the Stern-Geary equation [50]:

$$R_P = \frac{\beta_a \beta_c}{2.3(\beta_a + \beta_c) I_{corr}} \quad (4)$$

Where β_a and β_c are the anodic and cathodic Tafel slopes, respectively. The calculated R_p values confirmed the results obtained by the EIS characterization, which consisted of a lower resistance for Alloy#2, consequently leading to higher corrosion currents. After 100 hours of immersion, both alloys showed increased polarization resistance, in agreement with the trend observed by fitting of the EIS contributions. The obtained I_{corr} values were used to calculate the corrosion rates by using the following equation:

$$CR = \frac{K \cdot EW \cdot I_{corr}}{\rho} \quad (5)$$

Where I_{corr} is in $\mu A \cdot cm^{-2}$; EW is the equivalent weight, correspondent to 26.43 g/mol for Alloy#1 and 23.43 g/mol for Alloy#2; ρ is the density of the alloy, correspondent to 8.44 g/cm^3 for Alloy#1 and 8.22 g/cm^3 for Alloy#2; K is a constant, equal to 0.00327, including the Faraday constant and the conversion factor from $cm \cdot s^{-1}$ to $mm \cdot y^{-1}$. In agreement with the R_p trends, the corrosion rates decreased for both samples during the 100 hours of immersion and resulted lower for the Alloy#1.

Table 5. Fit results of the LPR data of the investigated Cu-Al-Mn-Ni-SMAs after 1 and 100 hours of immersion.

Measure	R_p ($\Omega \cdot cm^2$)	I_{corr} ($A \cdot cm^2$)	E_o (V)	Corrosion rate (mm/y)
Alloy#1-1 h	$1.716 \cdot 10^4$	$7.624 \cdot 10^{-7}$	-0.251	0.008
Alloy#1-100 h	$1.740 \cdot 10^4$	$6.633 \cdot 10^{-7}$	-0.251	0.007
Alloy#2-1 h	9368	$1.495 \cdot 10^{-6}$	-0.237	0.014
Alloy#2-100 h	$1.067 \cdot 10^4$	$1.210 \cdot 10^{-6}$	-0.246	0.011

The polarization curves were measured to study the shape of the cathodic and anodic branches and to identify the characteristic points. A similar behaviour was observed for both alloys, indicating that the rate of the overall corrosion process is controlled by the cathodic contribution, as can be seen

from the lower currents measured in the correspondent region for both samples (Figure 5). The cathodic branch describes the charge transfer at the metal/solution interface, followed by mass transport associated with oxygen diffusion to the surface of the electrode, which limits the corrosion process. The anodic region showed an active-passive behaviour highlighted by two peaks at -0.26 V and +0.015 V, compatible with the oxidation and dissolution processes of Cu and Ni. The measured currents decreased after the peak at +0.015 V suggesting the formation of insoluble corrosion products on the electrode surface, which have a protective effect and reduce the active dissolution of the alloy [51,52]. It is worth noting that the current decrease is not as relevant as in passive alloys, thus not providing a significant reduction of the corrosion rate. Alloy#2 additionally showed a current increase at +0.6 V, indicating the removal or solubilization of the corrosion products, leading to an increase in the dissolution rate of the alloy.

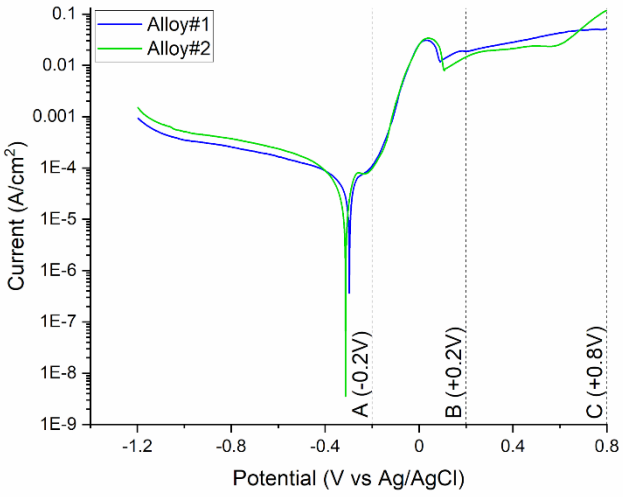

Figure 5. Polarization curves of the investigated Cu-Al-Mn-Ni-SMAs – the vertical dashed lines indicate the potentials at which polarizations were stopped to study the resulting corrosion products.

3.3 Post-corrosion characterization

Following the corrosion tests, the surfaces of the specimens were characterized using SEM-EDXS, micro-Raman spectroscopy and XRD to obtain morphological and compositional information on the

corrosion products. Figure 6 reports the SEM micrographs of the surfaces exposed for 100 hours at OCP and those polarized at different anodic potentials.

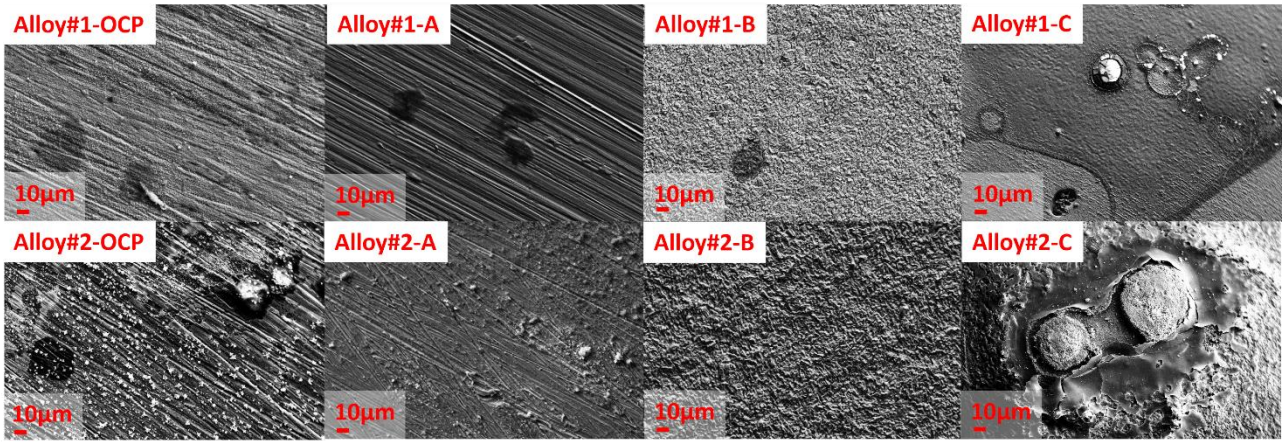

Figure 6. SEM micrographs of Cu-Al-Mn-Ni-SMAs surfaces after testing at OCP and different polarization potentials.

Table 6. Results of the EDXS chemical composition of the Cu-Al-Mn-Ni-SMA surfaces after testing at OCP and different polarization potentials.

Spectrum	O	Cl	Cu	Al	Mn	Ni
Alloy#1-OCP	60.9	6.7	20.2	8.5	2.4	1.3
Alloy#1-A	33.9	1.8	53.1	4.6	5.3	1.3
Alloy#1-B	7.3	-	91.8	-	0.9	-
Alloy#1-C	50.9	14.6	15.8	2.2	11.5	5.0
Alloy#2-OCP	24.2	8.0	56.3	6.2	1.9	3.4
Alloy#2-A	42.4	24.0	24.3	7.6	0.6	1.1
Alloy#2-B	20.8	0.4	63.1	9.8	2.1	3.8
Alloy#2-C	35.8	16.4	40.4	4.1	1.8	1.5

After 100 hours of exposure, localized pitting corrosion was not detected, and polishing lines are still visible on the surface of Alloy#1 (Figure 6), indicating the presence of a thin layer of corrosion products with chlorine in their composition, as highlighted by EDXS analysis (Table 6). This was

confirmed by XRD analysis (Figure 8, Alloy#1-OCP), which detected copper hydroxychloride [53], together with aluminium hydroxide, copper chloride and copper (I) oxide [54]. Phases related to the substrate alloy are still noticeable. Micro-Raman spectroscopy (Figure 7 and Table 7) also detected the copper-nickel hydroxychloride and both aluminium oxide and hydroxide, suggesting a partial dissolution of aluminum in the hydroxide form that could be caused by the weakly alkaline pH of the testing solution. Mn oxides were also detected in the Alloy#1, by both micro-Raman and XRD analyses.

The immersion for 100 hours of Alloy#2 led to visually increased corrosion compared to the previous sample (Figure 6). Pitting was not detected, being the corrosive process developing outward, resulting in the formation of a thick layer of corrosion products. The EDXS analysis highlighted an increased amount of chlorides compared to the previous sample (Table 6). Even the XRD analysis (Figure 8, Alloy#2-OCP) spotted the presence of a variety of compounds in agreement with the previous sample, with the addition of manganese oxide and a mixture of manganese/nickel oxide. The presence of manganese oxide was also detected by micro-Raman analysis (Table 7).

The key points of the polarisation curve were studied by analyzing the surfaces after the application of selected anodic potentials.

At point A, the surfaces appeared to be less attacked by corrosion compared to the samples exposed for 100 hours at OCP. The Alloy #1 sample is mainly characterized by an oxide coverage composed of copper oxides and copper chloride hydrate, showing a partial agreement with the observations on samples immersed at OCP.

Similar composition of the corrosion products was observed in Alloy#2, where also copper chloride and aluminium chloride hexahydrate were detected, in partial agreement with micro-Raman analysis. In fact, micro-Raman analyses identified the formation of copper (I) oxide, copper (II) chloride dihydrate, and copper (II) oxide on both samples, while the additional copper (I) chloride compound was found solely on Alloy#2. Overall, alloy#2 appeared to be characterized by a surface not entirely

covered by corrosion products. Site II (Figure 7, Alloy#2-A) did not yield any appreciable micro-Raman signal except for a peak of copper (I) chloride.

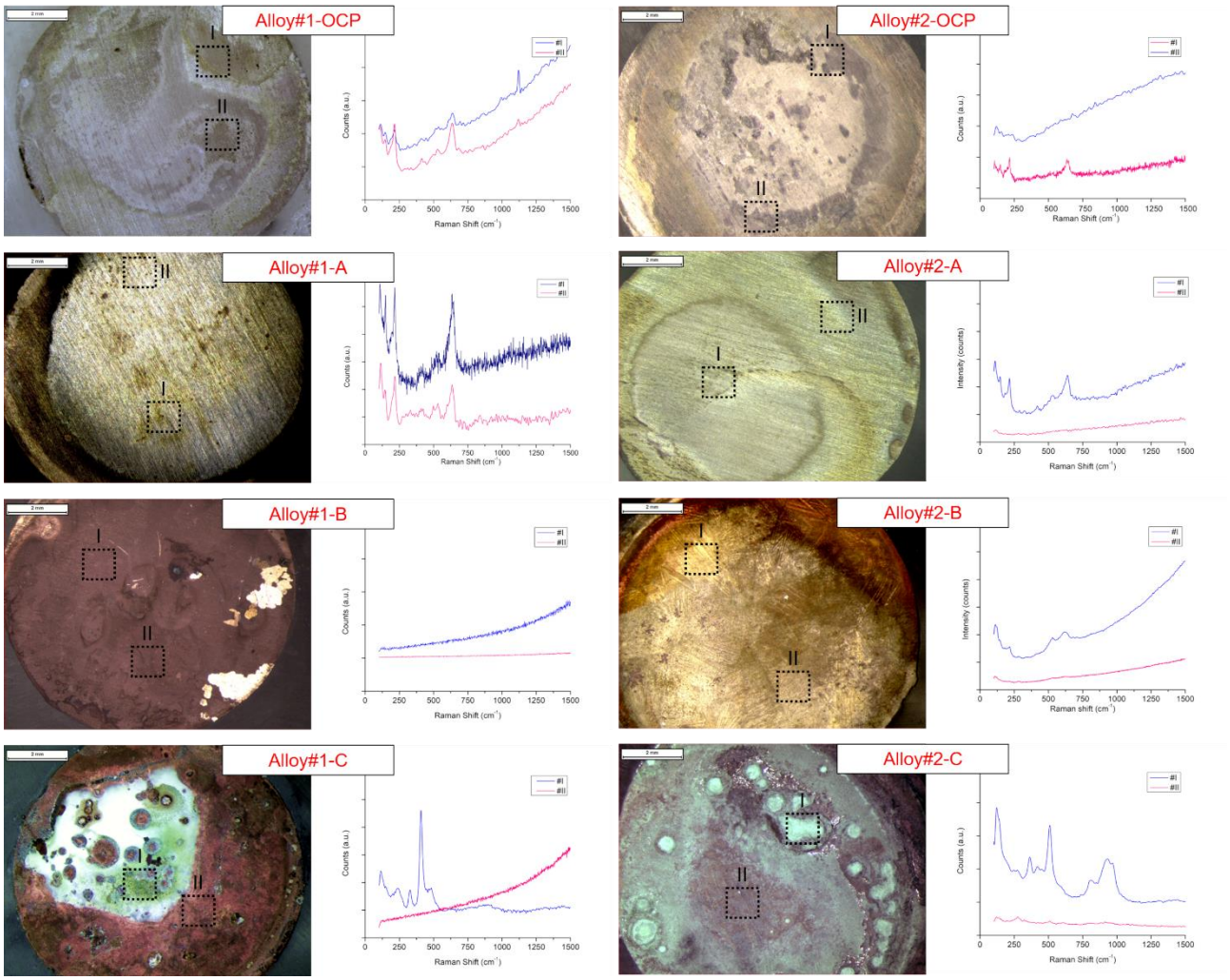

Figure 7. Post-experimental micro-Raman spectra of Cu-Al-Mn-Ni-SMAs and corresponding measurement position shown by stereomicroscopic images (6x magnification).

Table 7. Identification of Raman bands at measurement positions (compare with Figure 7).

Testing Condition	Alloy#1 – Micro-Raman shift	Alloy#2 – Micro-Raman shift
OCP	Site #I • Cu_2O (150, 224cm^{-1}) [55] • $Cu_2Cl(OH)_3$ (601 cm^{-1}) [56] • $(Cu,Ni)_2Cl(OH)_3$ (279 cm^{-1}) [56] • CuO (633 cm^{-1}) [55] Site #II • Cu_2O (417 cm^{-1}) [55] • MnO_2 (536 cm^{-1}) • $CuCl_2 \cdot 2H_2O$ (146, 215 cm^{-1}) [57] • Al_2O_3 and Mn_2O_3 (641 cm^{-1}) [58] • $Al(OH)_3$ (304 cm^{-1}) [59]	Site #I • Cu_2O (157, 221, 416 cm^{-1}) [55,60,61] • Mn_2O_3 (534 cm^{-1}) • $Al_2O_3/Al(OH)_3$ (Mixture Al oxides/ hydroxides) (583, 646 cm^{-1}) [62,63] Site #II • MnO_2 (665 cm^{-1}) [64] • $Cu_2Cl(OH)_3$ (123, 157 cm^{-1}) [56] • $(Cu,Ni)_2Cl(OH)_3$ (245, 279 cm^{-1}) [56] • $Al_2O_3/Al(OH)_3$ (Mixture Al oxides/ hydroxides) (387 cm^{-1}) [62,63]
A	Site #I • Cu_2O (144, 219, 419, 531 cm^{-1}) [55] • $CuCl_2 \cdot 2H_2O$ (117 cm^{-1}) [57] • CuO (633 cm^{-1}) [55] Site #II • Cu_2O (210, 526 cm^{-1}) [55] • $CuCl_2 \cdot 2H_2O$ (408 cm^{-1}) [57] • CuO (633 cm^{-1}) [55]	Site #I • Cu_2O (224, 410, 531 cm^{-1}) [55] • CuCl (154 cm^{-1}) [57] • CuO (638 cm^{-1}) [55] Site #II • $CuCl_2 \cdot 2H_2O$ (145) [57]
B	No Raman activity detected	Site #I • Cu_2O (526 cm^{-1}) [55] • $CuCl_2 \cdot 2H_2O$ (117, 215 cm^{-1}) [57] • $Al(OH)_3$ (615 cm^{-1}) [65] Site #II • CuO (289 cm^{-1}) [55]
C	Site #I • $CuCl_2 \cdot 2H_2O$ (238 cm^{-1}) [57] • $Cu_2Cl(OH)_3$ (121 cm^{-1}) [56] • $(Cu,Ni)_2Cl(OH)_3$ (401, 475 cm^{-1}) [56] • $Al(OH)_3$ (326 cm^{-1}) [65] • Site #II No Raman activity detected	Site #I • Cu_2O(145 cm^{-1}) [61] • $CuCl_2 \cdot 2H_2O$ (117-118, cm^{-1}) [57] • $Cu_2Cl(OH)_3$ (123, 513-514, 964 cm^{-1}) [57] • $(Cu,Ni)_2Cl(OH)_3$ (279 cm^{-1}) [56] • Al hydroxides (322, 426, 450, 455, 605, 782, 812, 875, 917, 930 cm^{-1}) [62] • Complex Cu-Cl corrosion products (815-817, 968 cm^{-1}) [57] • Mn oxides/hydroxides (358 cm^{-1}) [66] Site #II • $(Cu,Ni)_2Cl(OH)_3$ (279 cm^{-1}) [56]

When Alloy#1 was polarized to 0.8 V vs Ag/AgCl (point C), the grain boundaries were evidenced as they were subjected to etching. Additional deposits of corrosion products can be observed at the centre of such grains (Figure 6). A crack in the re-deposited copper coverage (red-brown colour) was observed after the polarization up to 0.8 V, as observed through the stereomicroscope image (Figure 7). Such a fracture exposes the alloy surface to a further corrosion process that leads to the formation of a significant amount of chlorides and hydroxides, which are well noticeable in the green-coloured parts of the specimen (site I, Figure 7). XRD analysis mainly detected copper and copper oxide. EDXS spotted an increased amount of chloride and nickel compared to the previous samples. Micro-Raman spectroscopy detected the presence of aluminium hydroxide and confirmed the EDXS observations by revealing copper- and copper-nickel hydroxychloride, similar to the sample immersed for 100 hours at OCP. On Alloy#2, a thicker layer of corrosion products was observed, characterized by cone-shaped formations, mainly noticeable by stereomicroscopic image in Figure 7 (Alloy#2-C). The EDXS analysis detected a high amount of chlorine due to the formation of copper hydroxychloride and copper nickel hydroxychloride as found by Micro-Raman spectroscopy, together with aluminum hydroxides. XRD analysis confirmed the presence of chlorides and also detected manganese dioxide, a mixture of manganese-nickel oxide, aluminium chloride hexahydrate, copper (I) oxide and the substrate composition.

Notably, copper re-deposition was only noticed in Alloy#1 and appears evident from the analysis of the stereomicroscopic images of Figure 7 (Alloy#1-B and -C). This behaviour may be clearly appreciable from the XRD results. Conversely, a higher amount of copper hydroxychloride and substrate signals were observed in Alloy#2, as noticeable, for instance, from the stereomicroscopic images of Figure 7 -Alloy#2-B, where the martensite structure is clearly visible.

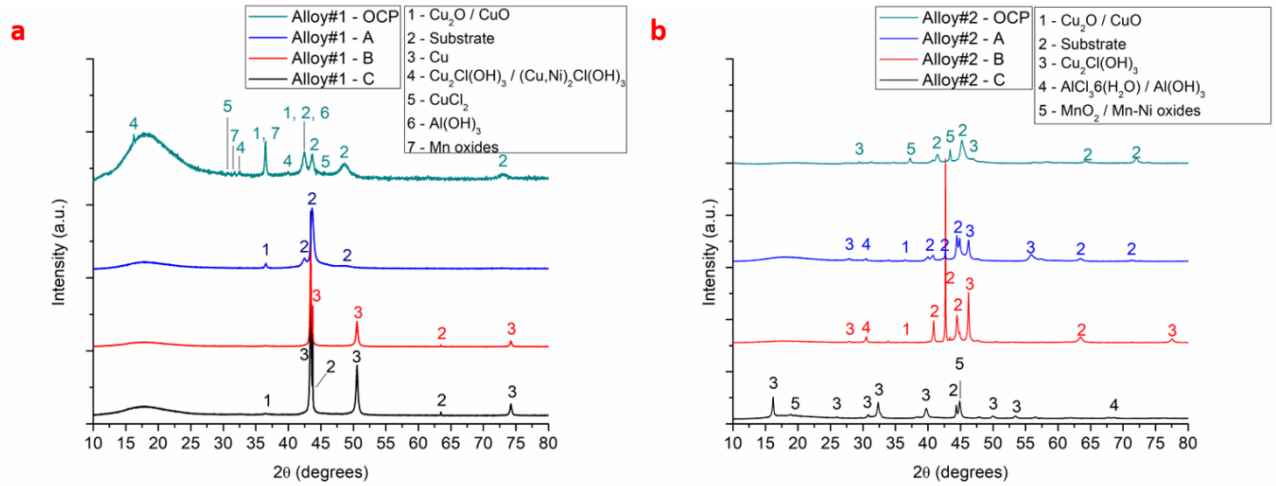

Figure 8. Post-experimental XRD analyses of Cu-Al-Mn-Ni-SMAs and phase characterization – (a) Alloy#1 and (b) Alloy#2.

4. Discussion

Microstructure

The research involved casting and homogenizing two Cu-Al-Mn-Ni-SMAs to achieve a wide transformation temperature range for potential SMA applications. Variations in aluminium, manganese, and nickel content resulted in different transformation temperatures and microstructures: entirely pseudoelastic (Alloy#1) and pseudoplastic (Alloy#2). The microstructural change was induced by a short homogenization heat treatment before testing. Previous studies have shown that the homogenization time had a negligible effect on the transformation temperatures of Alloy#1, while significant microstructural changes occurred rapidly. The localized formation of a secondary phase at the grain boundaries in Alloy#1 could be attributed to the microsegregation of elements [67]. However, for Alloy#2, previous studies showed a significant effect of homogenization time on the transformation temperatures, resulting in a morphology change of martensite. The martensitic structure in Alloy#2 was attributed to the higher aluminium content and lower manganese content in the chemical composition of the alloy.

Corrosion

The lower OCP values measured at the beginning of the experiment for Alloy#1 are due to the lesser aluminium and nickel content compared to Alloy#2. When OCP values shift to a higher level, it indicates a lower susceptibility to generalized corrosion. This is usually attributed to the formation of a passive layer on the surface of the sample, which can act as a protective barrier against corrosion [42]. The standard electrode potentials of the elements contained in the tested alloys are -0.16 V (Cu/Cu^{2+}), -0.23 V (Ni/Ni^{2+}), -1.18 V (Mn/Mn^{2+}), -1.66 V (Al/Al^{3+}), indicating that copper is the noblest and aluminium the least noble element, in this order copper > nickel > manganese > aluminium [68]. Therefore, aluminium, manganese, and nickel are more likely to be electrochemically oxidized before copper, leading to the formation of corrosion products on the surface, which act as a barrier to protect the surface and thus increase corrosion resistance. Post-experimental characterizations have shown that copper and aluminium promote the formation of the corresponding copper (I) oxide, copper (II) oxide, and alumina. However, copper chlorides, and aluminium hydroxide were also found, due to testing in sodium chloride aqueous solution, which is a particularly aggressive environment for copper and aluminium. In the presence of chlorides the formation of copper chloride ions is favoured by the following reactions 6 and 7 [48]:

$$Cu + Cl^- \rightarrow CuCl \quad (6)$$

$$CuCl + Cl^- \rightarrow CuCl_2^- \quad (7)$$

The detected copper hydroxychlorides results form the alternative reaction of copper or copper chloride following the respective reactions 8 and 9:

$$2Cu + O_2 + Cl^- + H_2O \rightarrow Cu_2(OH)_3Cl + OH^- \quad (8)$$

$$CuCl + O_2 + 4H_2O \rightarrow Cu_2(OH)_3Cl + HCl \quad (9)$$

The copper (I) oxide found on the surface is the result of the further reaction of the copper (II) chloride ion with water that can occur as follows :

$$CuCl_2^- + H_2O \rightarrow Cu_2O + 4Cl^- + 2H^+ \quad (10)$$

Manganese oxide can also form on manganese-containing alloys as a result of the pH increase according to the reactions 11 and 12 [31]:

$$Mn^{2+} + H_2O \rightarrow Mn(OH)_2 + 2H^+ \quad (11)$$

$$2Mn(OH)_2 + O_2 \rightarrow MnO_2 + 2H_2O \quad (12)$$

The nobler initial OCP of Alloy#2 results from the high nickel content and its high standard potential. The addition of such an element could have a positive effect on the corrosion behaviour by reducing the potential gap between the copper and the less noble elements present in the alloy, thus extending the galvanic series and mitigating the resulting galvanic currents. However, as Badawy et al. found, a high amount of nickel inhibits the formation of passive species and thus reduces corrosion resistance [36].

The corrosion mechanism at OCP has been clarified by EIS characterization. Figures 4c and d show the EEC diagrams superimposed on the interface characteristics to clarify their correspondences. For

both samples, EEC in the first 40 hours of the experiment was characterized by the presence of three time constants, including a Warburg element related to the electrochemical reactions controlled by the diffusion process. This contribution, due to a reversible dissolution-precipitation mechanism from the substrate, is used to explain the formation of a passive film when the substrate is still partially covered by corrosion products [49]. In fact, when the resistance value associated with the Warburg element is higher than the charge transfer resistance, it indicates that the corrosion products do not completely cover the surface of the sample and dissolution from the substrate is possible by following the reactions 6 and 7 [69]. The continuous increase in R_{ct} results from the increasing coverage of the sample, which is completed before 60 hours of immersion, when the Warburg contribution by EIS is no longer detectable because a film of corrosion products has formed, preventing metals from being dissolved into ions, as shown in figure 4d [48]. At this point, only dissolution of corrosion products can occur by their interaction with the solution. The increase in R_{ct} for both samples indicates an overall improvement in corrosion resistance over time due to the growth of the layer of corrosion products, as confirmed by LPR measurements. Comparing the R_p and I_{corr} values of the two alloys, it is found that the pseudoelastic alloy (Alloy#1) is superior to the pseudoplastic one (Alloy#2) in terms of corrosion resistance. This result could also be due to the higher amount of manganese in the Alloy#1 composition, favouring the formation of a stable layer of corrosion products. Additionally, the presence of the martensitic structure in Alloy#2 could have a role in enhancing the galvanic corrosion effect, thus decreasing the overall corrosion resistance [32,70].

Figure 9 compares the evolution in resistive contributions of impedance for both samples. The trend in charge transfer resistance (Figure 9a), which was similar for both samples during the first few hours of the experiment, changed as the surfaces reached complete coverage with corrosion products, highlighting the different properties of the growing layer. The tendency of R_{ct} to a plateau for Alloy#1 indicates stabilization of the passive layer, which also led to reaching a limiting thickness of the electrical double layer, as can be seen from the low and stable values of its effective capacitance. The low capacitance and n values of the film contribution indicate the formation of a dense and thin layer

on the surface of the sample [48,71]. The continuous increase in resistivity can be attributed to the increase in film thickness, which leads to an improvement in corrosion resistance.

For Alloy#2, the film resistance showed constant but lower values compared to the previous sample, leading to higher corrosion rates. The charge transfer resistance did not reach stability because of the continuous development of the corrosion product layer on the surface, which, however, contributed in the decrease of the corrosion rate, as measured by LPR. Post-experiment characterization detected the presence of insoluble compounds on the surface of the samples, supporting the deconvolution of EIS data by proposing a time constant related to a layer of corrosion products and the observed decrease in corrosion rates. The presence of soluble species confirmed a further interaction of the corrosion products with the solution, which led to dissolution processes driven by the pH and presence of chlorides.

Additionally, although the corrosion products were comparable in composition, their morphology, observed by SEM, resulted in inhomogeneous, confirming the absence of a compact layer.

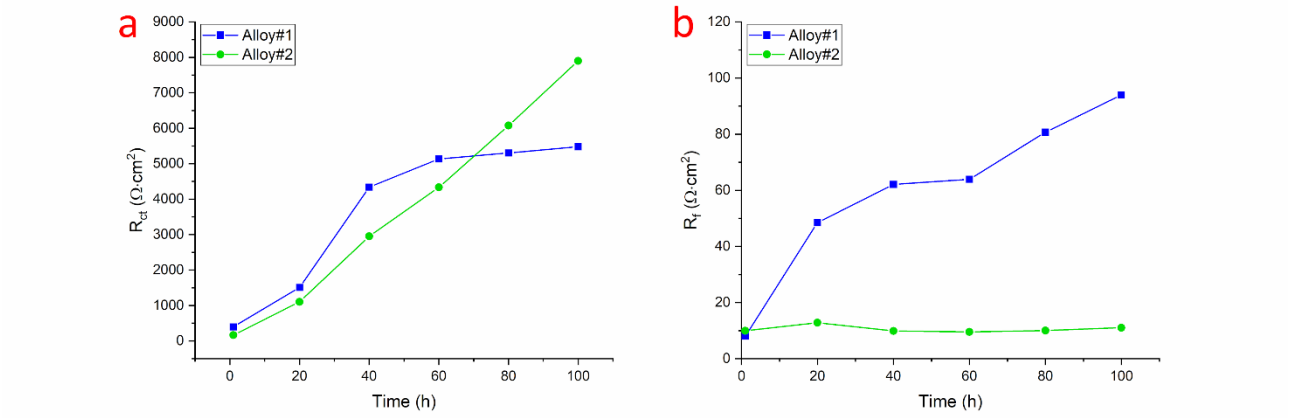

Figure 9. Evolution of the charge transfer resistance (a) and film resistance (b) depending on time derived from EIS measurements.

The polarization curves highlighted the cathodic control of the corrosion reactions for both alloys, which consists of oxygen reduction according to the following reaction:

$$O_2 + 2H_2O + 4e^- \rightarrow 4OH^- \quad (13)$$

Alloy#2 showed higher current density values in this part of the graph, indicating increasing activity toward oxygen reduction. This can be attributed to both composition and morphological features. On the one hand, the higher nickel content in the alloy could play a role in facilitating oxygen reduction by supporting the formation of a layered nickel oxyhydroxide structure, thus improving the kinetics of the reaction [72]. On the other hand, the fine microstructure associated to the presence of martensite increases the number of interfaces and the density of crystallographic defects [73]. This is thermodynamically beneficial for oxygen evolution activity compared to coarser grains with lower density of defects [74,75].

The anodic branch was characterized by a first inflection point after the Tafel region, where the formation of copper oxides and dissolution of copper into soluble copper (II) chloride ions is the dominant corrosion mechanism in both alloys. This was confirmed by polarizing the samples at -0.2 V vs Ag/AgCl, where post-experimental analysis revealed the presence of copper species resulting from the oxidation of copper in agreement with the reactions 6, 7 and 10.

The following peak, measured at 0.18 V vs Ag/AgCl, is due to further oxidation of aluminium, as indicated by the presence of aluminium hydroxide on the surface of Alloy#2 when polarized at 0.2 V vs Ag/AgCl. This potential also promoted the formation of copper oxides and hydroxychlorides, which, together with aluminium hydroxide, were responsible for the decrease in current density [51,76]. In contrast, Alloy#1 was completely covered by copper because of the metal re-deposition. In conclusion, at the higher applied polarization potential corresponding to 0.8 V vs Ag/AgCl, the surface of both samples appeared highly non-homogeneous due to the massive formation of corrosion products. The macroscopic areas where copper deposition occurred can be easily distinguished by regions covered by corrosion products consisting of copper chlorides and copper-nickel hydroxychlorides. This suggests that this potential also promoted the oxidation of nickel and its inclusion in the corrosion products. The martensitic structure led to the formation of a less protective

layer that grew inhomogeneously and caused the current rise at 0.6 V vs Ag/AgCl. The more homogeneous microstructure and the higher amount of manganese in the Alloy#1 composition provided the formation of a stable layer of corrosion products, which was confirmed by the trend of current density at high potentials.

Concluding, the absence of pitting on both types of samples, as evidenced by SEM analyses, confers reliability to the measured corrosion rates and suggests the potential applicability of the investigated alloys in chloride-affected environments. The formation of stable corrosion product layers results in less harmful consequences to the functional properties compared to localized attacks.

5. Conclusions

In this work, the corrosion behaviour of two Cu-Al-Mn-Ni SMAs in an aqueous sodium chloride solution was investigated by extensive electrochemical characterization and post-experiment analysis. The results highlighted that:

1) The corrosion mechanism started upon immersion in the test solution, regardless of the alloy microstructure, by a diffusion process and the formation of corrosion products that gradually covered the entire surface. Once complete coverage was achieved, the diffusion processes associated with the dissolution/re-deposition of copper were hindered by the corrosion products;
2) Manganese contributed to the improvement of the corrosion resistance by participating in the formation of insoluble oxides within the corrosion products layer. Higher Mn amounts in the pseudoelastic alloy led to lower corrosion currents at OCP and under polarization;
3) The martensitic structure of the pseudoplastic alloy resulted in increased activity for oxygen reduction, which contributed to the decrease of the corrosion resistance. The higher galvanic

currents, together with a lower amount of manganese, were responsible for the formation of an inhomogeneous and less protective layer of corrosion products.

In this research it was shown that the Cu-Al-Mn-Ni alloys investigated have the potential to be used as SMAs in chloride-affected environments, such as maritime applications or in automotive components that are exposed to chlorides, e.g. exposure of microactuators to road salt in winter. Based on the experimental results of this study, further investigations can be carried out, such as corrosion fatigue tests or field tests in which the samples are placed on offshore structures, near coastal areas, or guardrails of the motorway.

Acknowledgement

This work was kindly supported by the Federal Ministry for Economic Affairs and Climate Action. The investigated SMA materials were developed and optimized within the research project "Ertüchtigung von Cu-FGL" INNO-KOM VF 49VF210023 from the Forschungsgemeinschaft Werkzeuge und Werkstoffe e. V., Papenberger Straße 49, 42859 Remscheid, Germany.

References

[1] J. Mohd Jani, M. Leary, A. Subic, M.A. Gibson, Mater. Des. **2014**, 56, 1078.

[2] G.B. Olson, M. Cohen, Scr. Metall. **1975**, 9, 1247.

[3] W.M. Huang, Z. Ding, C.C. Wang, J. Wei, Y. Zhao, H. Purnawali, Shape memory materials, in: Mater. Today, **2010**: pp. 54–61.

[4] J. Perkins, ed., Shape Memory Effects in Alloys, Springer US, Boston, MA, **1975**.

[5] Shape Memory Alloys, Springer US, Boston, MA, **2008**.

[6] J. Van Humbeeck, Mater. Sci. Eng. A **1999**, 273–275, 134.

[7] K.. Melton, O. Mercier, Acta Metall. **1979**, 27, 137.

[8] G. Eggeler, E. Hornbogen, A. Yawny, A. Heckmann, M. Wagner, Mater. Sci. Eng. A **2004**, 378, 24.

[9] R.J. Wasilewski, S.R. Butler, J.E. Hanlon, D. Worden, Metall. Trans. **1971**, 2, 229.

[10] D. Hodgson, S. Russell, Minim. Invasive Ther. Allied Technol. **2000**, 9, 61.

[11] K.K. Alaneme, E.A. Okotete, Eng. Sci. Technol. an Int. J. **2016**, 19, 1582.

[12] R. Dasgupta, J. Mater. Res. **2014**, 29, 1681.

[13] E.M. Mazzer, M.R. da Silva, P. Gargarella, J. Mater. Res. **2022**, 37, 162.

[14] V. Recarte, R.B. Pérez-Sáez, J. San Juan, E.H. Bocanegra, M.L. Nó, Metall. Mater. Trans. A **2002**, 33, 2581.

[15] U. Sarı, İ. Aksoy, J. Alloys Compd. **2006**, 417, 138.

[16] S. Miyazaki, K. Otsuka, H. Sakamoto, K. Shimizu, Trans. Japan Inst. Met. **1981**, 22, 244.

[17] V. Novák, P. Šittner, D. Vokoun, N. Zárubová, Mater. Sci. Eng. A **1999**, 273–275, 280.

[18] Y. Sutou, T. Omori, R. Kainuma, K. Ishida, Mater. Sci. Technol. **2008**, 24, 896.

[19] Y. Sutou, T. Omori, J.J. Wang, R. Kainuma, K. Ishida, Mater. Sci. Eng. A **2004**, 378, 278.

[20] U.S. Mallik, V. Sampath, J. Alloys Compd. **2008**, 459, 142.

[21] R. Kainuma, S. Takahashi, K. Ishida, Metall. Mater. Trans. A **1996**, 27, 2187.

[22] Y. Sutou, R. Kainuma, K. Ishida, Mater. Sci. Eng. A **1999**, 273–275, 375.

[23] U.S. Mallik, V. Sampath, J. Alloys Compd. **2009**, 469, 156.

[24] S.N. Saud, E. Hamzah, T. Abubakar, M.K. Ibrahim, A. Bahador, J. Mater. Res. **2015**, 30, 2258.

[25] C.A. Canbay, Z.K. Genc, M. Sekerci, Appl. Phys. A **2014**, 115, 371.

[26] U. Sari, Int. J. Miner. Metall. Mater. **2010**, 17, 192.

[27] Z. Han, H. Zhao, Mater. Sci. Eng. A **2003**, 345, 8.

[28] W.A. Badawy, M.M. El-Rabiei, H. Nady, Electrochim. Acta **2014**, 120, 39.

[29] J.S. de Souza, M.C.L. de Oliveira, R.A. Antunes, R.A.G. da Silva, J. Mater. Res. Technol. **2022**, 16, 1213.

[30] A.O. MOGHADDAM, M. KETABCHI, R. BAHRAMI, Trans. Nonferrous Met. Soc. China **2013**, 23, 2896.

[31] S.N. Saud, E. Hamzah, T. Abubakar, H.R. Bakhsheshi-Rad, Trans. Nonferrous Met. Soc. China (English Ed. **2015**, 25, 1158.

[32] S.N. Saud, E. Hamzah, T. Abubakar, H.R. Bakhsheshi-Rad, M. Zamri, M. Tanemura, J. Mater. Eng. Perform. **2014**, 23, 3620.

[33] G.R. Holcomb, D.E. Alman, J. Mater. Eng. Perform. **2006**, 15, 394.

[34] J.S. Souza, C.R. Martins, L.S. Silva, R.A.G. Silva, Mater. Chem. Phys. **2022**, 282, 125945.

[35] H. Nady, N.H. Helal, M.M. El-Rabiee, W.A. Badawy, Mater. Chem. Phys. **2012**, 134, 945.

[36] W.A. Badawy, M.M. El-Rabiee, N.H. Helal, H. Nady, Electrochim. Acta **2010**, 56, 913.

[37] L. VRSALOVIĆ, I. IVANIĆ, S. KOŽUH, S. GUDIĆ, B. KOSEC, M. GOJIĆ, Trans. Nonferrous Met. Soc. China **2018**, 28, 1149.

[38] L. Vrsalović, I. Ivanić, S. Kožuh, B. Kosec, M. Bizjak, J. Kovač, U. Gabor, M. Gojić, Corros. Rev. **2019**, 37, 579.

[39] D. Vladikova, Electrochim. Acta **2002**, 47, 2943.

[40] B. BOUKAMP, Solid State Ionics **1986**, 20, 31.

[41] J. MACDONALD, L. POTTERJR, Solid State Ionics **1987**, 24, 61.

[42] R.F. Alves, R.A. Raimundo, B.A.S.G. Lima, D.F. Oliveira, R.A.C. de Santana, R.M. Gomes, C.J. de Araújo, J. Mater. Res. Technol. **2023**, 24, 6009.

[43] G. Ghiara, R. Spotorno, S. Delsante, G. Tassistro, P. Piccardo, P. Cristiani, Corros. Sci. **2019**, 157,.

[44] E. Barsoukov, J.R. Macdonald, Impedance Spectroscopy, **2005**.

[45] P. Canepa, G. Ghiara, R. Spotorno, M. Canepa, O. Cavalleri, J. Alloys Compd. **2021**, 851, 156937.

[46] G.J. Brug, A.L.G. van den Eeden, M. Sluyters-Rehbach, J.H. Sluyters, J. Electroanal. Chem. Interfacial Electrochem. **1984**, 176, 275.

[47] M. Khademi, D.P.J. Barz, Langmuir **2020**, 36, 4250.

[48] Y. Ding, R. Zhao, Z. Qin, Z. Wu, L. Wang, L. Liu, W. Lu, Materials (Basel). **2019**, 12,.

[49] X. Zhang, T. Cui, Q. Liu, Z. Dong, C. Man, J. Alloys Compd. **2021**, 858, 157685.

[50] M. Stern, A.L. Geary, J. Electrochem. Soc. **1957**, 104, 56.

[51] M. Gojić, L. Vrsalović, S. Kožuh, A. Kneissl, I. Anžel, S. Gudić, B. Kosec, M. Kliškić, J. Alloys Compd. **2011**, 509, 9782.

[52] A.V. Benedeti, P.T.A. Sumodjo, K. Nobe, P.L. Cabot, W.G. Proud, Electrochim. Acta **1995**, 40, 2657.

[53] K. Chen, D. Xue, J. Phys. Chem. C **2013**, 117, 22576.

[54] M. Chmielová, J. Seidlerová, Z. Weiss, Corros. Sci. **2003**, 45, 883.

[55] Y. Deng, A.D. Handoko, Y. Du, S. Xi, B.S. Yeo, ACS Catal. **2016**, 6, 2473.

[56] R.L. Frost, Spectrochim. Acta Part A Mol. Biomol. Spectrosc. **2003**, 59, 1195.

[57] R.L. Frost, P.A. Williams, J.T. Kloprogge, W. Martens, Neues Jahrb. Für Mineral. - Monatshefte **2003**, 2003, 433.

[58] Y. Liu, B. Cheng, K.-K. Wang, G.-P. Ling, J. Cai, C.-L. Song, G.-R. Han, Solid State Commun. **2014**, 178, 16.

[59] H. Mindivan, E. Sabri Kayali, H. Cimenoglu, Wear **2008**, 265, 645.

[60] H. Solache-Carranco, G. Juárez-Díaz, A. Esparza-García, M. Briseño-García, M. Galván-Arellano, J. Martínez-Juárez, G. Romero-Paredes, R. Peña-Sierra, J. Lumin. **2009**, 129, 1483.

[61] A.L. Ma, S.L. Jiang, Y.G. Zheng, W. Ke, Corros. Sci. **2015**, 91, 245.

[62] A. Lekatou, A.K. Sfikas, A.E. Karantzalis, D. Sioulas, Corros. Sci. **2012**, 63, 193.

[63] A. Kreta, M. Rodošek, L. Slemenik Perše, B. Orel, M. Gaberščck, A. Šurca Vuk, Corros. Sci. **2016**, 104, 290.

[64] T. Gao, H. Fjellvåg, P. Norby, Anal. Chim. Acta **2009**, 648, 235.

[65] E. Huang, A. Li, J. Xu, R.-J. Chen, T. Yamanaka, Geophys. Res. Lett. **1996**, 23, 3083.

[66] S. Bernardini, F. Bellatreccia, A. Casanova Municchia, G. Della Ventura, A. Sodo, J. Raman Spectrosc. **2019**, jrs. 5583.

[67] S. Belkahla, H. Flores Zuñiga, G. Guenin, Mater. Sci. Eng. A **1993**, 169, 119.

[68] C. Tatar, Thermochim. Acta **2005**, 437, 121.

[69] M. yang YIN, Z. LI, Z. XIAO, Y. PANG, Y. ping LI, Z. yan SHEN, Trans. Nonferrous Met. Soc. China (English Ed. **2021**, 31, 1012.

[70] W.R. Osório, A. Cremasco, P.N. Andrade, A. Garcia, R. Caram, Electrochim. Acta **2010**, 55, 759.

[71] M.H. Ata, H.M.A. El-Lateef, M. Elrouby, Surfaces and Interfaces **2021**, 26, 101384.

[72] A. Singh, T. Schneller, I. Valov, I.B. Singh, A.K. Srivastava, R. Waser, J. Catal. **2020**, 384, 189.

[73] S. Van Petegem, D. Segers, V. Pelosin, J. Kuriplach, Appl. Phys. A Mater. Sci. Process. **2005**, 81, 1039.

[74] H.K. Park, H. Ahn, T.H. Lee, J.Y. Lee, M.G. Lee, S.A. Lee, J.W. Yang, S.J. Kim, S.H. Ahn, S.Y. Kim, C. Lee, E.S. Park, H.W. Jang, Small Methods **2021**, 5, 2000755.

[75] C. Huang, K. Sasaki, D. Senthil Raja, C. Hsieh, Y. Wu, J. Su, C. Cheng, P. Cheng, S. Lin, Y. Choi, S. Lu, Adv. Energy Mater. **2021**, 11,.

[76] S.N. Saud, E. Hamzah, T. Abubakar, H.R. Bakhsheshi-Rad, Mater. Corros. **2015**, 66, 527.

Figure legend

Figure 1. Optical micrographs and XRD spectra of (a) Alloy#1 and (b) Alloy#2, both polished and etched. Arrows in (a) indicate the secondary phase visible at the grain boundaries.

Figure 2. Open Circuit Potential of Cu-Al-Mn-Ni SMA samples depending on time.

Figure 3. Nyquist plot of the electrochemical impedance spectroscopy (a, c) and the Bode representations (b, d).

Figure 4. DIA temporal plots of EIS measured at 1 h and 60 h of Alloy#1 (a) and Alloy#2 (b), and the proposed EECs (c, d).

Figure 5. Polarization curves of the investigated Cu-Al-Mn-Ni-SMAs – the vertical dashed lines indicate the potentials at which polarizations were stopped to study the resulting corrosion products.

Figure 6. SEM micrographs of Cu-Al-Mn-Ni-SMAs surfaces after testing at OCP and different polarization potentials.

Figure 7. Post-experimental Raman spectra of Cu-Al-Mn-Ni-SMAs and corresponding measurement position shown by stereomicroscopic images (6x magnification).

Figure 8. Post-experimental XRD analyses of Cu-Al-Mn-Ni-SMAs and phase characterization – (a) Alloy#1 and (b) Alloy#2.

Figure 9. Evolution of the charge transfer resistance (a) and film resistance (b) depending on time derived from EIS measurements.